Design and Analysis of a Frontside Series/Parallel Piezoelectric Resonator-Based DC–DC Converter

Wen-Chin B. Liu, *Graduate Student Member, IEEE*, and Patrick P. Mercier, *Senior Member, IEEE*

***Abstract*—Piezoelectric (PR)-based dc–dc converters present an attractive opportunity to reduce converter costs and size, while simultaneously enhancing efficiency. However, the efficiency of a conventional PR-based dc–dc converter experiences a significant decline when operating outside the nominal 2:1 conversion ratio, diminishing appeal for applications demanding low voltage conversion ratios (VCRs), specifically, VCR $\leq$ 0.2. To enable improved efficiency at low conversion ratios, this article introduces a frontside series/parallel piezoelectric resonator (FSPPR) dc–dc converter, where a series/parallel switched-capacitor network is merged with the baseline PR-based topology in a hybird arrangement for an additional 2:1 down conversion. In this article, the operation principle and behavior of the proposed FSPPR converter are mathematically analyzed, simulated, and verified, and then the FSPPR converter, along with a baseline PR-based converter prototype, is designed and built utilizing commercial off-the-shelf lead zirconate titanate PRs. Experimental measurements reveal a peak efficiency of 95.27% at a conversion ratio of 48/10V, representing a noteworthy 14% efficiency improvement in comparison to the codesigned baseline PR-based converter.**

***Index Terms*—Piezoelectric resonator, resonant converter, soft-charging operation, switched capacitor (SC), zero-voltage switching (ZVS).**

I. Introduction

THE increasing demands for high-efficiency, lightweight, and low-cost miniaturized power converters are starting to highlight the limitations posed by magnetic passive elements. While conventional electromagnetic-based converters are renowned for their fast response, ease of control, and high power capability, the sublinear scaling property of magnetic components [1], [2], [3], where the magnetic size reduces nonlinearly with an increase in frequency, limits the pathway toward converter miniaturization. Consequently, there is a growing interest in exploring alternative energy storage forms, materials, and devices to replace magnetic components [4], [5], [6], [7], encompassing diverse manifestations, such as kinetic, elastic, and electrostatic energy storage.

Piezoelectric devices are one of the prospective candidates, as they can be easily batch fabricated at low cost, offer thin planar form factors, and, importantly, offer linear frequency/volume scaling properties. These devices store energy in the form of elastic energy and can be implemented in multiport or single-port forms: piezoelectric transformers (PTs) and piezoelectric resonators (PRs), respectively. PTs were previously found applications in push-pull, class E, and half/full-bridge converters [8], [9], [10], [11], [12] implemented along with magnetic components. To eliminate the use of magnetics, magnetic-less PT-based converters have also been explored [13], [14], [15]. However, due to efficiency limitations and zero voltage switching (ZVS) constraints [16], [17], [18], PTs have not gained widespread adoption yet. PRs, on the other hand, have emerged as particularly promising alternatives to inductors in dc–dc converters. Recent works demonstrated both step-up and step-down magnetic-free converters with promising gains in efficiency [19], [20], [21] and power density [22], [23], [24], thereby affirming the effectiveness of PRs.

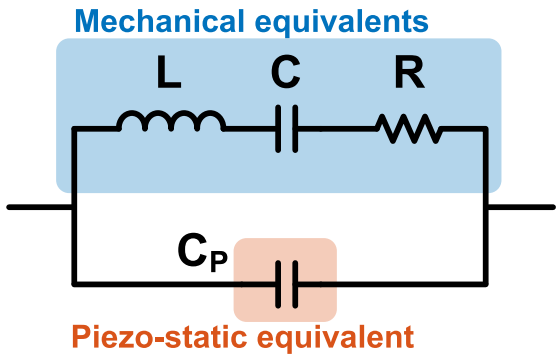

Fig. 1. Butterworth Van-Dyke equivalent model for piezoelectric resonators.

Though PRs are identified as good alternatives to inductors, they do not serve as direct replacements. The Butterworth Van-Dyke (BVD) model [25], as depicted in Fig. 1, is a commonly adopted electrical equivalent model for PRs, where the model is comprised of mechanical components, R, L, and C, and a piezo-static capacitor, C_P. Notably, the equivalent model functions as a dc block component, making PRs unsuitable for conventional inductor-based converters. Hence, modified topologies and modulation laws are required to achieve optimal operation of PR-based converters.

There are a variety of inductor-less PR-based dc–dc converters reported [19], [20], [21], [26] for step-up or step-down conversion. This work specifically focuses on step-down conversion with voltage conversion ratios (VCRs), donated as VCR =

Received 14 March 2024; revised 31 May 2024 and 16 August 2024; accepted 30 August 2024. Date of publication 10 September 2024; date of current version 12 December 2024. This work was supported by Power Management Center (PMIC) an NSF I/UCRC under Grant 2052809. Recommended for publication by Associate Editor M. A. E. A. E. Andersen. *(Corresponding author: Patrick P. Mercier.)*

The authors are with the Department of Electrical and Computer Engineering, University of California at San Diego, San Diego, CA 92093 USA (e-mail: brianliu.pe@gmail.com; pmercier@ucsd.edu).

Color versions of one or more figures in this article are available at https://doi.org/10.1109/TPEL.2024.3457867.

Digital Object Identifier 10.1109/TPEL.2024.3457867

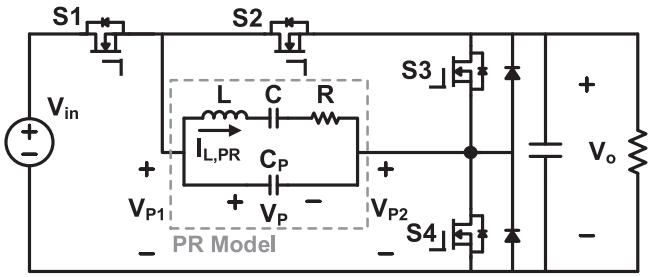

Fig. 2. Baseline step-down PR-based converter [20].

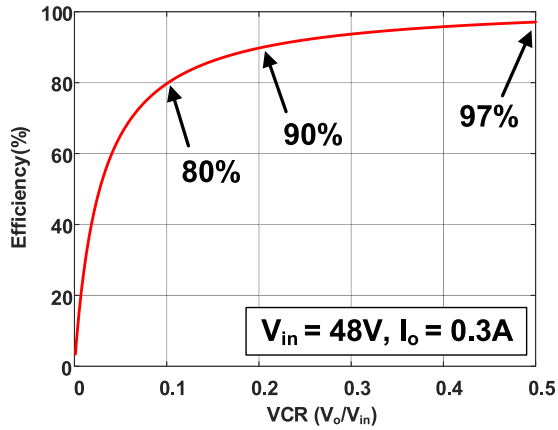

Fig. 3. Efficiency curve example of baseline step-down PR-based converter (plotted based on analysis in [20]).

V_o/V_{in}, less than 0.25. Among the high-step-down topologies, the baseline PR-based dc–dc converter, as shown in Fig. 2, was reported to be one of the most efficient topologies [20] for VCRs ≤ 0.5 scenarios. By operating the PR in the inductive resonating region, ZVS across all switches and soft-charging of the piezo-static capacitor, C_P, can be achieved, leading to low overall losses.

However, the baseline PR-based converter achieves its optimal efficiency at a VCR of 0.5, with performance degrading as the operations deviate from the optimal point, as shown in Fig. 3. At a VCR of 0.5, the efficiency of the baseline PR-based converter reaches an impressive 97%, but decreases dramatically as VCR decreases, reducing to 90% and 80% at 0.2 and 0.1 VCR, respectively. Unfortunately, a great number of step-down dc–dc applications require a much larger conversion ratio (i.e., VCR ≤ 0.2), and the efficiency degradation limits the appeal of the baseline PR-based step-down converter adoption in such applications.

To overcome the efficiency challenge under large step-down conversion scenarios popularized by many applications, i.e., computing, automotive, and consumer electronics, this work, as an extension of [27], introduces the design and analysis of the Frontside Series/Parallel Piezoelectric Resonator (FSPPR) converter. In the FSPPR converter, a switched capacitor (SC) network is integrated into the conventional PR-based step-down converter as shown in Fig. 4, in a similar manner to a 2:1

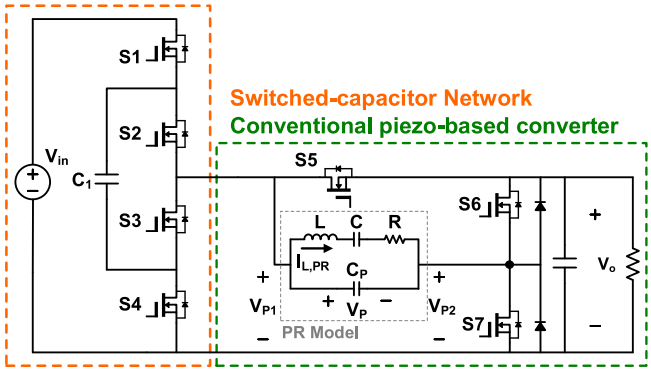

Fig. 4. Circuit diagram of series/parallel piezoelectric resonator converter.

series/parallel SC hybrid Buck converter. By leveraging the advantages of the series/parallel SC network, the optimal efficiency point of the converter can be shifted downward while retaining most of the benefits associated with the baseline PR-based converter, including ZVS, soft charging, and voltage regulation capabilities. Moreover, owing to the inductive operation of PRs, the flying capacitor within the SC network undergo soft charging/discharging across all operation ranges, thereby further reducing overall losses. Note that other possible hybrid PR-based dc–dc topologies can be imagined, including the work in [28], [29], [30].

In the selection of PR materials and vibration modes for this work, two materials with corresponding vibration modes emerge: disk-shaped lead zirconate titanate (PZT) PRs employing radial/thickness vibration [19], [26], [27], [31], [32] and rectangular-shaped lithium niobate ($LiNbO_3$ or LNO) PRs utilizing thickness vibration [7], [21], [23]. Given that the focus of this article is in discussing the FSPPR hybrid PR-based dc–dc topology, custom PR materials are not considered, and instead commercial-off-the-shelf (COTS) PRs are targeted. Here, disk-shaped PZT PRs are chosen for their regular production and standard size availability. Regarding vibration modes, the thickness mode, wherein applied and induced electric fields are parallel, exhibits a higher vibrating frequency (a few MHz) with severe spurious modes [7], [21], [33], which deteriorates performance; on the other hand, the radial mode, whose fields are perpendicular, presents a cleaner response [7], [19], [27] in its inductive region, preserving optimal performance. Therefore, a disk-shaped PZT PR in radial mode is selected in this work.

The rest of this article is organized as follows: The operation principle is illustrated in Section II. In Section III, the topological analysis is conducted, including the PR charge utilization, VCR, steady-state interval approximation, and efficiency estimation. In Section IV, the PR selection and mounting strategies are discussed based on calculation and measurement results. In Section V, the FSPPR converter prototype with a PZT PR in a disc-shaped radial vibration mode is physically built along with the baseline PR-based converter, shown in Fig. 2, where both of them share the same components and PCB design to demonstrate the advantage of the proposed topology.

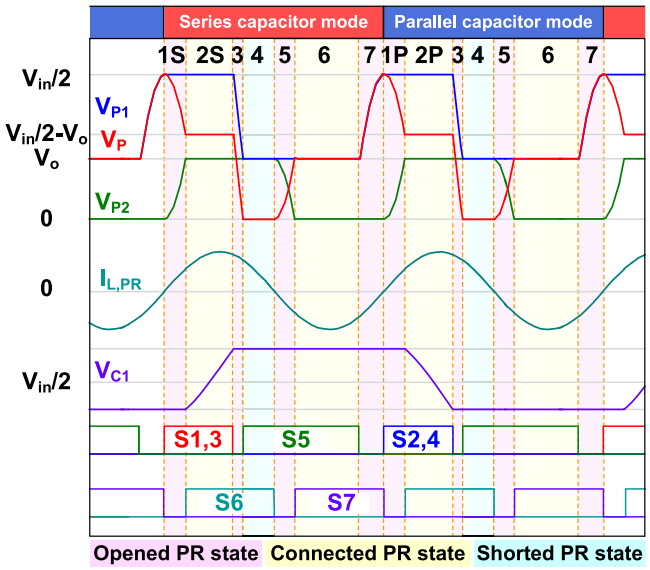

Fig. 5. Operation waveforms of series/parallel piezoelectric resonator converter.

II. Series/Parallel Piezoelectric Resonator DC–DC Converter

The circuit diagram of the proposed FSPPR converter is shown in Fig. 4, where the PR is represented by the BVD model. In the BVD model, R, L, and C refer to the mechanical vibration of the PR, while C_P is the piezo-static capacitor of the PR. From the equivalent model, the PR can be operated in either the inductive or capacitive regions, depending on the operation frequency. To achieve ZVS, the PR is forced to operate in its inductive region in the proposed topology, where the detailed operations will be discussed in the following paragraphs.

In front of the PR stage, a 2:1 SC network is merged as the input stage, which can be viewed as a prestep-down stage where switches S1-4 operate between series and parallel SC modes to the PR stage. In the series SC mode, S1 and S3 are turned ON, placing the flying capacitor, C_1, in series with the piezo-based stage; on the other hand, in the parallel SC mode, S2 and S4 are turned ON, placing C_1 in parallel with the piezo-based stage. In this configuration, the flying capacitor, C_1, is clamped to half the input voltage, resulting in the reduction of voltage stress on switches in the SC network and the effective input voltage to the piezo-based stage, which is now approximately half the input voltage. This is a similar benefit that flying capacitor multilevel hybrid inductive buck converters enjoy. Therefore, the equivalent voltage seen across the PR stage is halved compared to the baseline PR-based converter.

It should be noted that switches S1-4in the FSPPR topology effectively replace switch S1 in the baseline topology, and thus the SC stage is integrated into the PR stage with no additional cascaded losses presented. In addition, any control scheme applicable to the baseline converter could also be applied to the FSPPR converter. This will be explored in future work.

The operation waveforms and phases are depicted in Figs. 5 and 6. The FSPPR converter operates through seven individual

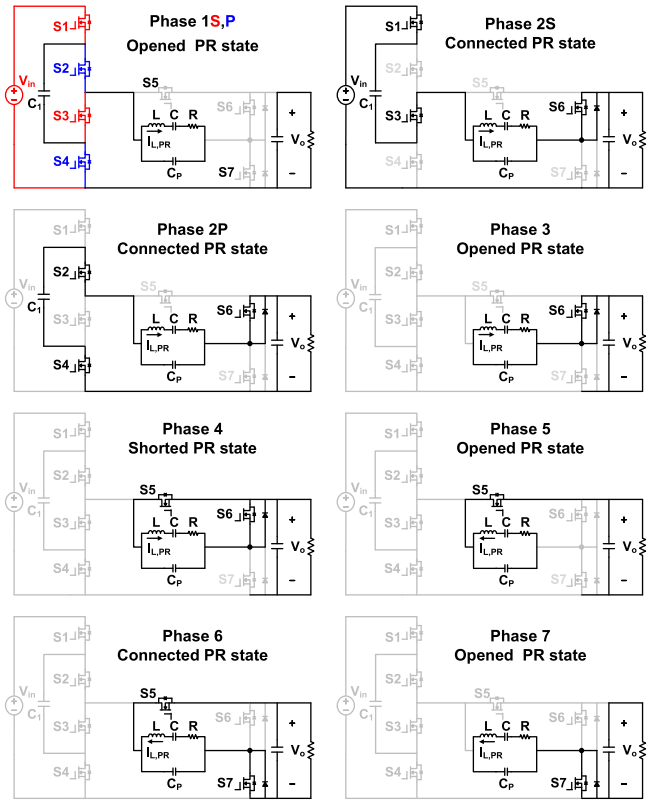

Fig. 6. Operation phases of series/parallel piezoelectric resonator converter.

phases in a sequential manner, employing two alternative modes: series capacitor mode and parallel capacitor mode. Across these seven phases, the piezoelectric resonator (PR) can be in one of three connection states:

1) *Connected PR state*: In this state, the PR is connected to either the input source, the output load, or both, forming a loop in which energy is delivered to output while the PR stores or releases energy.
2) *Shorted PR state*: In this state, the PR is shorted by the external switches, and the resonant current, $I_{L,\mathrm{PR}}$, circulates through the switches.
3) *Opened PR state*: In this state, the PR is opened, and the resonant current, $I_{L,\mathrm{PR}}$, circulates within PR through the piezo-static capacitor, C_P, allowing soft-charging/discharging of the capacitor to achieve ZVS in the subsequent phase.

As illustrated in Fig. 6, the PR is configured as an opened PR state in phases 1S and 1P where the piezo-static capacitor, C_P, is softly discharged by the inductive PR current, $I_{L,\mathrm{PR}}$. The phase ends when V_{P2} reaches V_o, enabling ZVS for S6. In phase 1S, the flying capacitor, C_1, is set to the up (series) configuration, while in the subsequent cycle, in phase 1P, C_1 operates in the down (parallel) configuration. In either case, S6 is activated once the drain-to-source voltage of S6 reaches zero, establishing a connection between the PR and the output and initiating phases 2S and 2P.

During phase 2S (series operation), the PR transfers energy from the input to the output while softly charging the flying

TABLE I
VOLTAGE ACROSS THE PR IN EACH PHASE

1S,P	2S,P	3	4	5	6	7
Open	$V_{\text{in}}/2 - V_o$	Open	0	Open	V_o	Open

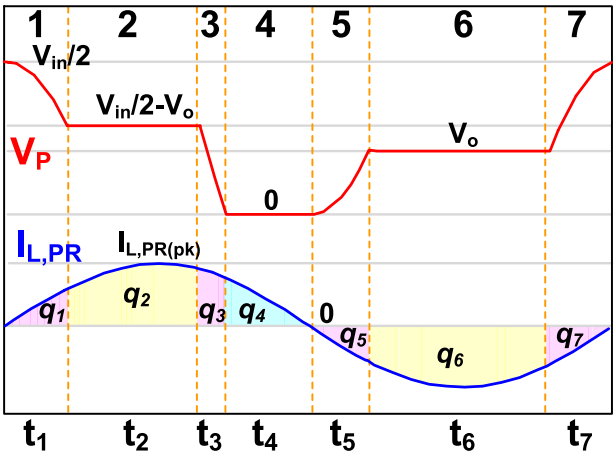

Fig. 7. Waveforms of a PR cycle.

capacitor (C_1), whereas phase 2P (parallel operation) involves the soft discharge of C_1 through $I_{L,\text{PR}}$ and delivers the energy to the output. Subsequently, in phase 3, switches S1–4 are all deactivated, placing the PR in an opened state, whereby $I_{L,\text{PR}}$ discharges C_P until $V_{P1} = V_o$, enabling ZVS for S5. Once $V_{P1} = V_o$, phase 4 begins, wherein both S5 and S6 are turned ON, shorting the PR to maintain the continuity of the resonant current. Phase 4 ends as $I_{L,\text{PR}}$ crosses zero and reverses its polarity. At this point, S6 is switched OFF, returning the PR in the opened state again, and phase 5 begins. During phase 5, $I_{L,\text{PR}}$ once again softly charges C_P, causing V_{P2} to decrease until it reaches zero, enabling ZVS turn-ON of S7. As soon as $V_{P2} = 0$, S7 is activated, connecting the PR to both the output and ground, releasing the stored energy to the load. Phase 7 begins with the deactivation of S5, placing the PR in the opened state, where C_P is softly charged by $I_{L,\text{PR}}$. This phase concludes when V_{P1} reaches V_{in}, thereby minimizing switching losses across S1, 3/S2, 4 in the following SC cycle.

The voltage across the PR in each phase over a cycle is shown in Table I.

III. STEADY-STATE OPERATION ANALYSIS

This section includes mathematical derivations and discussions of the VCR, charge transfer, resonant current, and time duration approximations, with the aim of comprehending the behavior, operation, and performance of piezoelectric resonators in the proposed FSPPR converter. Finally, the loss breakdown and efficiency estimation are presented.

A. VCR and PR Utilization

Fig. 7 illustrates the steady-state waveforms over a PR cycle in the proposed system. Due to the merged 2:1 SC network, the input voltage applied to the PR is half the input voltage rather than the full input voltage in the baseline PR-based converter. During steady-state operation, the piezoelectric resonator must adhere to the principles of conservation of charge (CoC) and conservation of energy (CoE) to maintain charge and energy balance [20], [26]. Therefore, the CoC of the PR mechanical capacitor, C, and the piezo-static capacitor, C_P, must hold in (1) and (2), where q_n is the charge in phase n

$$q_1 + q_2 + q_3 + q_4 + q_5 + q_6 + q_7 = 0 \tag{1}$$

$$q_1 + q_3 + q_5 + q_7 = 0. \tag{2}$$

By substituting (2) into (1), a balance in charge transfer between the connected and shorted states is revealed, yielding the following expression:

$$q_2 + q_4 + q_6 = 0. \tag{3}$$

On the other hand, only the connected states, phases 2 and 6, transfer energy, and hence the CoE must hold

$$E_2 + E_6 = V_2 q_2 + V_6 q_6 = (V_{\text{in}}/2 - V_o)\, q_2 + V_o q_6 = 0. \tag{4}$$

Then, inserting (3) into (4) using $q_6 = -(q_2 + q_4)$, the VCR of the FSPPR converter can be found as

$$0 \le \frac{V_o}{V_{\text{in}}} = \frac{1}{2}\frac{q_2}{2q_2 + q_4} \le \frac{1}{4}. \tag{5}$$

The VCR is observed to depend on the ratio of charge in the connected state (phase 2) to the shorted state (phase 4) within the positive cycle of $I_{L,\text{PR}}$. Assuming that the charge in the opened states (phases 1 and 3) is small and negligible, a maximum VCR of 0.25 is achieved when phase 2 spans the entire positive cycle of $I_{L,\text{PR}}$, indicating the complete utilization of the positive cycle for energy transfer. Conversely, a minimum VCR of 0 is obtained when phase 4 occupies the entire positive cycle, signifying no energy is sourced from the input. Notably, the VCR range is halved compared to the baseline PR-based converter presented in [20], owing to the inclusion of the series/parallel SC network.

The PR utilization factor, K, was first introduced in [20], and serves as an evaluation metric for how efficient the PR is used in a given topology with a specific phase sequence, regardless of materials, sizes, loss coefficients, etc. This factor is defined based on the concept of effective charge transfer, representing the portion of the charge in the connected and shorted states that ultimately contributes to the output. It should note that K is a topology/operation-sequence-related parameter, which is different from the PR-material-related electromechanical coupling factor, k_p.

Here, the PR utilization factor of the FSPPR converter can be defined as

$$K = \frac{|q_2| + |q_6|}{|q_2| + |q_4| + |q_6|}. \tag{6}$$

Substituting (3) and (4) into (6), the PR utilization factor can be rearranged in terms of V_{in} and V_o, which is shown as follows:

$$0.5 \le K = \frac{V_{\text{in}}}{2\,(V_{\text{in}} - 2V_o)} \le 1. \tag{7}$$

According to (7), K equals 1 when the VCR reaches its maximum value of 0.25, and, conversely, K equals 0 when VCR equals its minimum value, 0, implying that PR is most efficient at the maximum conversion ratio in the FSPPR converter where the duration of the resonant current circulating phase, phase 4, is minimum. In contrast, as the VCR reduces, K reduces as well, indicating inefficient utilization of the PR. Comparing to the baseline PR-based converter in [20], (5) and (7) show that the optimal efficiency is shifted down from the conversion ratio of 0.5 to 0.25.

B. Charge Transfer and PR Resonant Current

To derive the PR resonant current, $I_{L,\text{PR}}$, for the upcoming time duration and efficiency analysis, the total charge transferred and stored in the PR must be addressed first. There are two parts of charge transferred or stored in the PR: 1) the charge in connected and shorted state, Q_{CS}, and 2) the charge used to soft-charge/discharge C_P to achieve ZVS, Q_{ZVS}. The total charge can be expressed as follows:

$$Q_{\text{total}} = Q_{\text{CS}} + Q_{\text{ZVS}} = \frac{I_o}{Kf} + 2C_P V_{pp} \tag{8}$$

where V_{pp} is the voltage swing over C_P in a cycle and is notated as $V_{\text{in}}/2$ in the FSPPR converter.

On the other hand, the total charge can also be expressed in terms of $I_{L,\text{PR}}$ as

$$Q_{\text{total}} = 2\int_0^{\frac{1}{2f}} i_{L,\text{PR}}(t)dt \tag{9}$$

where

$$i_{L,PR}(t) = I_{L,\text{PR}(pk)} \sin(\omega t).$$

By equating the (8) and (9), the amplitude of the PR resonant current, $I_{L,\text{PR}(pk)}$, can be derived

$$I_{L,\text{PR}(pk)} = \frac{\pi}{2}\left(\frac{I_o}{K} + fC_P V_{\text{in}}\right). \tag{10}$$

C. Steady-State Phase Duration Approximation

For an accurate estimate of the performance and behavior in the proposed converter, it is essential to determine the steady-state duration in each phase. With the PR resonant current derived above, the steady-state phase duration can be obtained by integrating the charges in each phase. In Fig. 7, t_{1-7} represents the time duration in each phase. In this analysis, $V_{\text{in,PR}}$ is used to represent the effective input voltage of the piezo-based stage, which is half of the input voltage, $V_{\text{in}}/2$, in the FSPPR converter.

In phases 1S, and 1P, the resonant current discharges C_P from $V_{\text{in,PR}}$ to $V_{\text{in,PR}} - V_o$, and, therefore, the voltage difference over C_P in phase 1 can be written as follows:

$$\Delta V_{C_P(t_1)} = -V_o = \frac{1}{C_P}\int_0^{t_1} -i_{L,\text{PR}}(t)dt. \tag{11}$$

In phase 2, the PR is in the connected state, delivering energy to the output while storing energy in the PR. Based on the CoE in (4) and the loss due to the PR, the charge, q_2, in phase 2 can be rearranged as (12) where P_{loss} represents the losses in the PR

$$q_2 = \frac{P_o + P_{\text{loss}}}{V_{\text{in,PR}} f} = \int_0^{t_2} -i_{L,\text{PR}}(t + t_1)dt. \tag{12}$$

In phase 3, the PR is in the opened state and discharges C_P from $V_{\text{in}} - V_o$ to 0. As a result, the voltage difference over C_P in phase 3 can be written as follows:

$$\Delta V_{C_P(t_3)} = V_{\text{in,PR}} - V_o = \frac{1}{C_P}\int_0^{t_3} -i_{L,\text{PR}}(t + t_1 + t_2)dt. \tag{13}$$

In phase 4, the PR resonant current is freewheeling in a shorted loop, which ends when $I_{L,\text{PR}}$ reverses its polarity at the end of the positive cycle. Hence, the duration of phase 4, t_4, is given by the following:

$$t_4 = \frac{1}{2f} - t_1 - t_2 - t_3. \tag{14}$$

In phase 5, again, the PR is in the opened state, and $I_{L,\text{PR}}$ charges C_P from 0 to V_o; hence, the voltage across C_P can be written as follows:

$$\Delta V_{C_P(t_5)} = V_o = \frac{1}{C_P}\int_0^{t_5} -i_{L,\text{PR}}\left(t + \frac{1}{2f}\right)dt. \tag{15}$$

In phases 6 and 7, phase 6 is a connected state that transfers energy from the PR to the output, while phase 7 is an opened state where $I_{L,\text{PR}}$ charges C_P from V_o to V_{in}. Therefore, the time duration of phase 7 can be derived in (16) by solving the voltage difference over C_P in phase 7. On the other hand, since the duration of phases 5, 6, and 7 is a half cycle, the duration of phase 6 can be found from t_5, and t_7 in (17).

$$t_7 = \frac{1}{f} - t \tag{16}$$

where,

$$\Delta V_{C_P(t_7)} = V_{in,PR} - V_o = \frac{1}{C_P}\int_t^{\frac{1}{f}} -i_{L,PR}(t)dt$$

$$t_6 = \frac{1}{2f} - t_5 - t_7. \tag{17}$$

By solving (11)–(17), the time duration of each phase can be expressed as follows:

$$\begin{cases} t_1 = \frac{1}{\omega}\cos^{-1}\left(1 + \frac{-\omega C_P V_o}{I_{L,\text{PR}(pk)}}\right) \\ t_2 = \frac{1}{\omega}\cos^{-1}\left(\cos(\omega t_1) - \frac{2\pi(P_o + P_{\text{loss}})}{V_{\text{in,PR}} I_{L,\text{PR}(pk)}}\right) - t_1 \\ t_3 = \frac{1}{\omega}\cos^{-1}\left(\cos[\omega(t_1 + t_2)] + \frac{-\omega C_P (V_{\text{in,PR}} - V_o)}{I_{L,\text{PR}(pk)}}\right) - t_1 - t_2 \\ t_4 = \frac{1}{2f} - t_1 - t_2 - t_3 \\ t_5 = \frac{1}{\omega}\cos^{-1}\left(\frac{\omega C_P V_o}{I_{L,\text{PR}(pk)}} - 1\right) - \frac{1}{2f} \\ t_6 = \frac{1}{2f} - t_5 - t_7 \\ t_7 = \frac{1}{f} - \frac{1}{\omega}\cos^{-1}\left(1 - \frac{\omega C_P (V_{\text{in,PR}} - V_o)}{I_{L,\text{PR}(pk)}}\right) \end{cases}. \tag{18}$$

According to (18), it can be observed that the time duration of phase 2, t_2, can be used to control the power delivered to the output as well as the output voltage, which matches the feedback control method in [34], where t_2 is used to achieve voltage regulation.

To have an accurate time duration calculation, the operation frequency, ω, in (18) must be known. However, due to the variable frequency operation of the PR-based converter, the actual operating frequency varies between the resonant frequency (f_r) and the antiresonant frequency (f_{ar}), complicating the determination of an exact operating frequency beforehand. While a model for predicting the operating frequency has been reported in [35], it is not analytically solvable. Here, given that a PZT PR with a high-quality factor (ranging from 600 to 2000 [19], [20], [27], [31], [36]) is typically employed and the operating frequency approaches the PR resonant frequency, f_r, as output power level or losses increase, a simple and quick approximation could be made by putting f_r into (18) for early-stage analysis. It is worth noting that this assumption is made based on a good electro-mechanical coupling factor and quality factor of the piezoelectric devices, which allows the f_r and f_{ar} to be close, and as a result, the frequency variation does not span across a large frequency range. The quality factor, Q, is defined as $\sqrt{L/C}/R$.

D. Loss Analysis and System Efficiency

Once the value of $I_{L,\text{PR}(pk)}$ and the time duration of each phase have been calculated, the losses of the converter can be determined accordingly. The losses in the FSPPR converter can be divided into three main categories: 1) PR losses, 2) switching losses, and 3) conduction losses. Note that the ESR losses of capacitors and driving losses, $P_{\text{dri}} = Q_g V_{\text{gs}} f_{\text{sw}}$, of power MOSFETS are excluded in this work.

The PR losses contain dielectric, piezoelectric, and elastic losses; however, since the dielectric and piezoelectric losses are typically much smaller than elastic losses, these two types of losses can be ignored [37]. The elastic losses are the mechanical motion losses, represented by the mechanical resistor, R, in the BVD model. Therefore, the PR losses are given by the following:

$$P_{l\text{oss,PR}} = \frac{1}{2} I^2_{L,\text{PR}(pk)} R. \tag{19}$$

The switching losses occur only in switches S1–S4 of the SC network since the remaining switches achieve ZVS in steady-state operation. Here, a simplified loss estimation is used, as shown in (20), where $V_{\text{ds}(n)}$ in (20) represents the drain-to-source voltage in switch n (S1–S4), and C_{loss} is the lumped output capacitance at the drain-to-source nodes, which is a function of drain-to-source voltage. More accurate switching loss calculations can be found in [38]

$$P_{l\text{oss,SW}} \approx C_{\text{loss}} V^2_{\text{ds}(n)} f_{\text{sw}}. \tag{20}$$

The conduction losses occur during the PR-connected and PR-shorted states, specifically in phases 2, 4, and 6, as depicted in Figs. 5 and 6. There are no conduction losses in phases 1, 3, 5, and 7 due to the internal circulation of the PR in the opened state. Assuming ideal operation conditions where the ON/OFFtiming of S1–S7 perfectly matches, and the ON-resistance of switch n is consistent ($R_{\text{on}(n)}$), the total conduction losses and losses of each switch can be expressed as (21) and (22), respectively. Here, n represents the label of the switch (S1–S7), and the root-mean-square (RMS) current of each switch is given by (23), where $I_{\text{rms},ph(k)}$ denotes the RMS current of each phase, k,(phases 2, 4, and 6). Note that the time duration for each phase can be calculated using either the resonant frequency approximation or the accurate frequency extracted from simulation software, such as Simulink. Unless explicitly stated otherwise, the subsequent calculations employ the approximation method.

$$P_{\text{loss,cond}} = \sum_{n=1}^{7} P_{\text{loss,cond}(n)} \tag{21}$$

$$P_{\text{loss,cond}(n)} = I^2_{\text{rms}(n)} R_{\text{on}(n)} \tag{22}$$

$$I_{\text{rms}(n)} = \begin{cases} I_{\text{rms},ph2}/\sqrt{2}, & 1 \le n \le 4 \\ \sqrt{I^2_{\text{rms},ph4} + I^2_{\text{rms},ph6}}, & n = 5 \\ \sqrt{I^2_{\text{rms},ph2} + I^2_{\text{rms},ph4}}, & n = 6 \\ I_{\text{rms,ph6}}, & n = 7 \end{cases} \tag{23}$$

where

$$I_{,ph(k)} = \begin{cases} \sqrt{\frac{1}{T_{\text{sw}}} \int_0^{t_2} i^2_{L,\text{PR}} (t + t_1)\, dt}, & k = 2 \\ \sqrt{\frac{1}{T_{\text{sw}}} \int_0^{t_4} i^2_{L,\text{PR}} \left(t + \sum_{i=1}^{3} t_i\right) dt}, & k = 4 \\ \sqrt{\frac{1}{T_{\text{sw}}} \int_0^{t_6} i^2_{L,\text{PR}} \left(t + \sum_{i=1}^{5} t_i\right) dt}, & k = 6. \end{cases}$$

Finally, the system efficiency can be built based on the above-mentioned losses, as shown as follows:

$$\eta = \frac{P_o}{P_o + P_{\text{loss,PR}} + P_{\text{loss,SW}} + P_{\text{loss,Cond}}}. \tag{24}$$

E. Mathematical Model Verification

This section focuses on verifying and comparing the mathematical models proposed in Section III with MATLAB Simulink simulations. Then, the proposed model is used for the efficiency comparison of the FSPPR and baseline PR-based converter in the following section. It should be noted that the parameters employed in both the calculation and simulation are identical to those used in the measurements, as detailed in Table V.

To verify the time duration model (18), the operation waveforms are calculated and simulated, as depicted in Fig. 8. Here, the calculated waveforms are built based on the time duration model, where the time durations are individually calculated and applied to the modulation laws for the waveform representation. In addition, the calculation results based on both the accurate and approximated frequencies are presented in Fig. 8. Here, the accurate frequency is the same as the operation frequency in the simulation, f_{sim}, whereas the approximated frequency is the resonant frequency, f_r by assuming that the operation is in the vicinity of f_r. The analysis reveals that when $f_{\text{sw}} = f_{\text{sim}}$, the calculated waveforms are well-matched with the simulations, and when $f_{\text{sw}} = f_r$, there is a small phase shift over time due to the small frequency discrepancy. Nonetheless, the amplitudes of $I_{L,\text{PR}}$ in both cases closely approximate the simulation results. Therefore, the time duration model, (18), demonstrates its utility in estimating PR behavior during preliminary assessments.

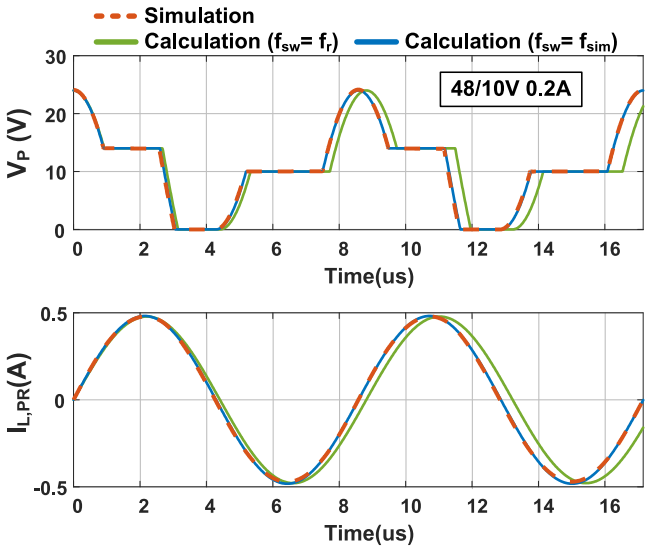

Fig. 8. Comparison of Operational waveforms in simulation and calculation.

TABLE II
SYSTEM EFFICIENCY MODEL VERIFICATION OF FSPPR CONVERTER AT 48/10 V, 0.2 A

Parameters	Calulation (approx.)	Simulation	Error (%)
$I_{rms(S1,3)}$	137.0 mA	136.5 mA	0.32
$I_{rms(S2,4)}$	137.0 mA	136.4 mA	0.41
$I_{rms(S5)}$	235.4 mA	236.2 mA	-0.36
$I_{rms(S6)}$	210.9 mA	210.9 mA	-0.01
$I_{rms(S7)}$	220.1 mA	220.2 mA	-0.01
$I_{L,PR(pk)}$	476.4 mA	480.6 mA	-0.88
Efficiency	96.17%	96.21%	-0.04

Following the verification of (18), the system loss model, particularly the root-mean-square current for each switch derived from (18), can be further verified. The comparison of simulation and calculation results at a 48–10 V, 0.2 A output scenario is shown in Table II, where the frequency approximation ($f_{sw} \approx f_r$) is applied to the calculation results. This table reveals an excellent agreement between calculated and simulated results, with errors under 1%, even when the switch frequency approximation is considered. The difference in efficiencies rises from the omission of node capacitance that is being charged and discharged during the opened PR states, diode conduction loss, and frequency approximation in the calculation. It is important to note that values in the table are rounded to the nearest first and second decimal places, and the error is computed using exact values.

F. Topological Comparison

This analysis compares the FSPPR with its precursor, the baseline PR-based converter. The VCR range, PR utilization factor, and the peak PR resonant current are elaborated in Table III. The variables $V_{\text{in,PR}}$ and $V_{o,\text{PR}}$ denote the equivalent PR input and output voltages during operation, while V_{in} and V_o denote that input and output voltages of the entire converter, and V_{pp} corresponds to the peak swing over the PR.

TABLE III
COMPARISON OF BASELINE PR-BASED CONVERTER AND FSPPR CONVERTER

	Baseline PR	FSPPR
VCR	$0 \le \text{VCR} \le 0.5$	$0 \le \text{VCR} \le 0.25$
PR charge utilization (K)	$0 \le \frac{V_{\text{in,PR}}}{2(V_{\text{in,PR}} - V_{o,\text{PR}})} \le 1$	
Optimal PR charge utilization (K_{opt})	$K = 1$ (VCR = 0.5)	$K = 1$ (VCR = 0.25)
Peak PR resonant current	$\pi\left(\frac{P_o}{2\text{KV}_{o,\text{PR}}} + f_{\text{sw}}\, C_P V_{\text{pp}}\right)$	
$V_{\text{in,PR}}$	V_{in}	$V_{\text{in}}/2$
$V_{o,\text{PR}}$	V_o	V_o
$V_{P(p-p)}$	V_{in}	$V_{\text{in}}/2$

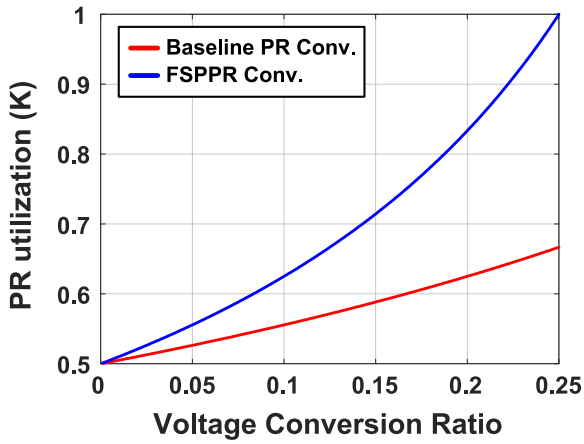

Fig. 9. PR utilization factor comparison of the FSPPR and baseline PR-based converters.

The PR utilization factor comparison is then plotted, as illustrated in Fig. 9, based on Table III. The FSPPR converter exhibits an enhanced utilization of the piezoelectric resonator throughout its operable VCR range (low VCRs), attributed to a reduced input voltage applied to the PR, implying potentially enhanced efficiencies in high step-down applications. That is, due to the SC conversion in the FSPPR converter, $V_{\text{in,PR}}$ is reduced and, as a result, the equivalent VCR of the PR itself, VCR_{PR}, is closer to 0.5, identified as its optimal efficiency point [20]. However, this is a tradeoff employed for overall conversion ratios restricted to below 0.25. In other words, the baseline PR-based converter is capable of a wider operation range, and thereby the baseline PR-based converter could be used for a VCR range between 0.5 and 0.25 while the FSSPR is more beneficial at VCRs below 0.25.

Upon comparing the VCR and K with the verification of the system loss and efficiency models, Fig. 10 shows the efficiency comparison of the FSPPR and baseline PR-based converters

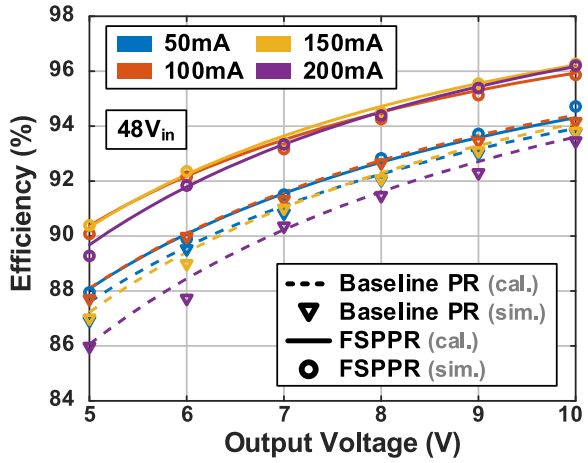

Fig. 10. Efficiency comparison of the FSPPR and baseline PR-based converters.

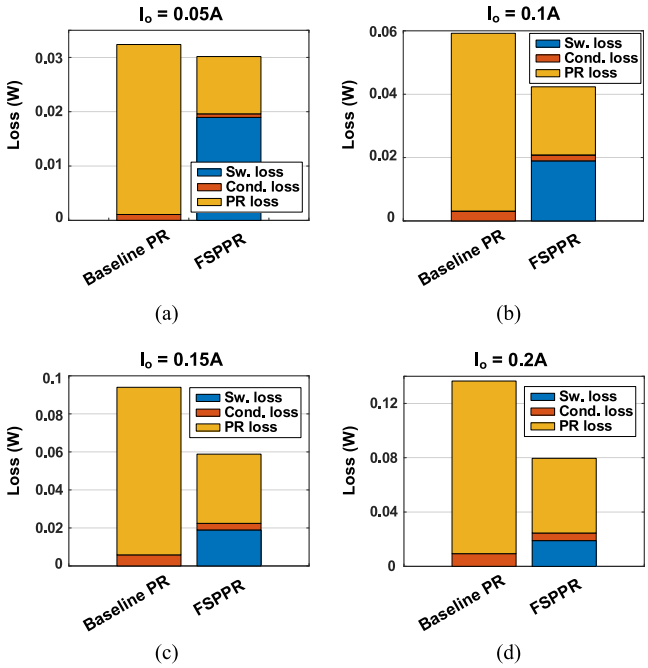

Fig. 11. Loss breakdown comparison at 48/10 V condition. (a) 48 V/10 V/0.05 A. (b) 48 V/10 V/0.1 A. (c) 48 V/10 V/0.15 A. (d) 48 V/10 V/0.2 A.

at a 48 V input voltage with different output voltages and currents, where the efficiencies are calculated and simulated with the parameters shown in Table V. It can be observed that, in all scenarios, the FSPPR converter outperforms the baseline PR-based converter with increasing efficiency advantages as the output current/power increases.

Fig. 11 shows the loss breakdowns of the baseline PR-based converter and the FSPPR converter at 48/10 V input/output voltage with different output conditions in Fig. 10. It can be seen that there is no switching loss presented in the baseline PR-based converter, while the FSPPR converter shows switching loss due to the SC network. Despite this, the FSPPR converter still presents a lower overall loss because the equivalent VCR of the PR stage in the FSPPR converter is much closer to its optimal operating point of 0.5; consequently, the PR current ($I_{L,\mathrm{PR}}$) and PR losses are reduced. The benefit of the SC network becomes more advantageous as the output current/power goes to a higher level. However, it should be noted that under extremely light load conditions, when switching losses start to dominate the overall losses, the baseline PR-based converter may exhibit higher efficiency than the FSPPR converter.

IV. Piezoelectric Resonator Selection

Understanding the physical properties of PRs and their relationship with the BVD electric equivalent model is crucial for the performance analysis of PR-based converters. This work specifically focuses on analyzing disk-shaped PRs in radial vibration mode.

Among PR materials for power electronic applications, two primary contenders emerge: PZT and lithium niobate ($\mathrm{LiNbO_3}$). These materials exhibit remarkably high mechanical quality factor (Q_m) and electromechanical coupling factor (k), critical parameters for achieving high-efficiency converters. However, since this study focuses on commercially available piezoelectric resonators with standard-fabricated sizes, $\mathrm{LiNbO_3}$ is excluded due to its custom-design-only availability. According to [31], the PIC181 material showcases excellent area loss and mechanical loss attributes, making it an ideal candidate for this work. Another promising candidate is C213 material, but it is exclusively fabricated upon custom orders with extended lead times of several months, rendering it, strictly speaking, not COTS. Hence, it is also ruled out from the list.

Before deciding on the size of disk-shaped PRs, understanding the limitations associated with specific sizes and their impact on overall performance, such as efficiency, is important. To address these concerns, insights can be gained through a BVD equivalent model, which serves as a simplified behavioral model. The BVD model of PR is illustrated in Fig. 2, where the R, L, and C represent the mechanical components related to elastic loss and mechanical vibrations. In addition, C_P is the piezo-static capacitor. The parameters of the BVD model for a disk-shaped PR can be found in [37], and are shown in (25)–(30) where the resonant and antiresonant frequencies, f_r and F_{ar}, can be found from the resonance of C_P, C, and L.

$$C_P = \varepsilon_{33}^T \left(1 - k_p^2\right) \frac{A}{l} \tag{25}$$

$$C = \frac{2\left(1+\sigma^E\right)}{X_h^2 - \left(1 - \left(\sigma^E\right)^2\right)} \frac{k_p^2}{1-k_p^2} C_P \tag{26}$$

$$L = \frac{a^2 \rho s_{11}^E \left(1-\sigma^E\right)}{2C_P} \frac{1-k_p^2}{k_p^2} \frac{X_h^2 - \left(1-\left(\sigma^E\right)^2\right)}{X_h^2} \tag{27}$$

$$R = \frac{1}{Q}\sqrt{\frac{L}{C}} \tag{28}$$

$$f_r = \frac{X_h}{2\pi a \sqrt{\rho s_{11}^E \left(1 - \left(\sigma^E\right)^2\right)}} \tag{29}$$

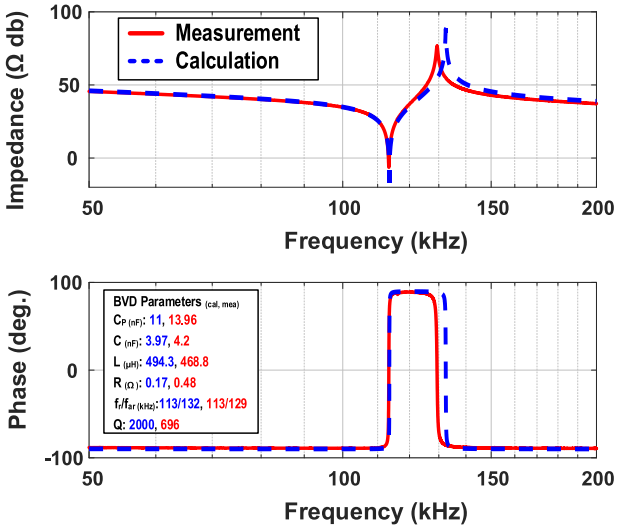

Fig. 12. Calculated and measured PR impedance spectrum comparison of the disk-shaped radial-mode piezoelectric resonator in a size of 20/0.2 mm (diameter and thickness) and PIC181 material.

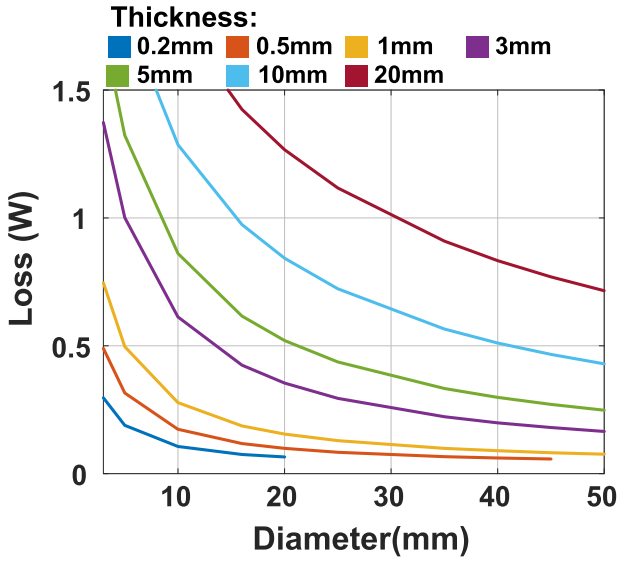

Fig. 13. Overall FSPPR converter losses with different PR diameter and thickness size (PIC181 material).

TABLE IV
EFFECT OF DIAMETER AND THICKNESS IN BVD MODEL

Parameters	Increase of diameter	Increase of thickness
f_r	Decrease(-)	No change (=)
C_P	Increase(+)	Decrease(-)
C	Increase(+)	Decrease(-)
L	No change (=)	Increase(+)
R	Decrease(-)	Increase(+)
$V_{PR,max}$	No change (=)	Increase(+)

$$f_{ar} = \sqrt{\frac{1+\left(\frac{2(1+\sigma^E)}{X_h^2-(1-(\sigma^E)^2)}-1\right)k_p^2}{1-k_p^2}}\, f_r. \tag{30}$$

Here, ϵ_{33}^T is the dielectric constant, k_p is the electromechanical coupling factor, A is the area of the PR, l is the thickness of the PR, σ^E is Poisson's ratio, a is the radius of the PR, ρ is the density of the PR material, s_{11}^E is the compliance constant, Q_m is the mechanical quality factor, ω_{sw} is the operating frequency, $\tan(\delta)$ is the dielectric loss factor, and X_h is the wave number, which is the solution for the boundary condition of motion displacement in the disk-shaped PR [37].

With the equations above and the selected material chosen, the physical parameters, e.g., the size of PRs, can be translated into the electrical representatives for further analysis, such as loss analysis. For example, Fig. 12 shows the calculated and measured PR impedance with PIC181 material in size of 20/0.2 mm, which shows a decent alignment between measurement and calculation implying the usefulness of the equation (25)–(30) for performance evaluation. The impact of diameter and thickness on the BVD model is summarized in Table IV. From this table, it can be seen that the resonant frequency solely depends on the diameter of PRs. This implies that smaller PRs can be utilized for higher operating frequencies. In contrast, the mechanical resistor, R, which is the primary source of loss in the PR, decreases with an increase in diameter and increases with an increase in thickness. Therefore, to minimize R in a given material, the PR should have a maximum diameter and minimum thickness, respectively. However, when the diameter and thickness are both maximized and minimized, both the piezo-static capacitor, C_P becomes significant. Besides, the f_r also varies with different diameters. These, consequently, increase the Q_{total} in (8) as well as the amplitude of the resonant current, $I_{L,PR(pk)}$, in (10). As a result, there exists an optimal range for the PR selection, which can be found by minimizing the total loss of the system.

Fig. 13 shows the total loss of the FSPPR converter with various PR sizes using the PIC181 material at 48/10 V, 0.3A, where the available PR sizes are obtained from the standard dimension table provided by PI ceramic. It can be found that, at a given thickness, a larger diameter leads to a lower overall loss; conversely, at a given diameter, a larger thickness results in a higher overall loss. This observation perfectly aligns with the physical model discussion above, indicating that minimizing losses requires minimizing the thickness and maximizing the diameter.

It should be noted that the PR size obtained from loss minimization is not always area/volume favorable as the loss reduction often saturates beyond a certain point with an increase in size. For instance, in Fig. 13, the loss of (0.5/45) mm PR size is slightly smaller than that of the (0.2/20) mm PR size, with losses of 57 mW and 65 mW, respectively. However, the area is significantly increased with areas of 0.16 cm^2 and 0.03 cm^2, respectively. Therefore, an alternative optimization method should be employed when the area becomes a critical factor in PR selection. One commonly used figure of merit (FOM) is the area-loss FOM, which is the product of losses and area, given by FOM $=$ loss $\times$ Area, with a minimal efficiency constraint. By minimizing the FOM with constraints, an optimal size can be found for the desired specification. It is important to note that apart from efficiency and area/volume considerations,

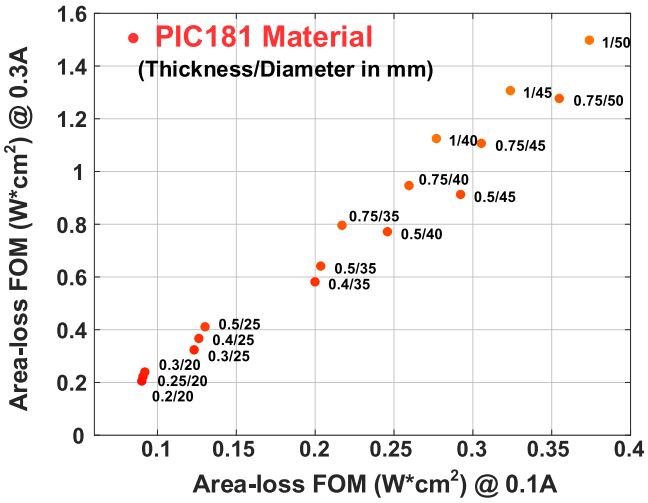

Fig. 14. Area-loss FOM comparison of PIC181 material with different sizes.

there are also hard limitations to be taken into account, such as the maximum voltage limitation, where the safe operating area for PZT material typically does not exceed 1 kV/mm, and the maximum current limitation, as described in [5].

Fig. 14 shows the area-loss FOM comparison for various available PIC181 PR sizes [36] at a 48/10 conversion ratio with 0.1 A and 0.3 A output in the x/y-axis, with an efficiency constraint of 95%. It can be found that the size of (0.2/20) mm exhibits the most favorable area-loss performance, and hence, the size of (0.2/20) mm PR is adopted in this work.

Aside from the material and sizing considerations, in practical design, thermal performance is critical for piezoelectric devices as the piezoelectric properties vary with temperature, potentially altering its behavior. However, due to the limited current density and power handling capabilities of the COTS PRs at present, which are not specifically designed for power applications, only a small amount of loss is dissipated in the PRs, given low output power, in this work. Thus, the thermal performance is not considered in this article. Nevertheless, when the COTS PRs are optimized for power electronic applications, which will involve higher output current and power in the future, the thermal behavior should be carefully considered.

V. Experimental Verification

A prototype of the FSPPR converter incorporating a piezoelectric resonator has been designed and built based on the aforementioned analysis and discussions and is shown in Fig. 15. The prototype can function as either a FSPPR or baseline PR-based converter, specifically noted in Fig. 15, enabling a fair performance comparison. The experimental parts and parameters are listed in Table V. In the implementation, a disk-shaped, radial vibration mode PR made of PIC181 material with a thickness and diameter of (0.2/20) mm is adopted. In addition, GaNFETs are applied to the prototype for their excellent switching/conducting characteristic, minimizing overall losses in the system. The prototype is digitally controlled by a DSP controller operating in an open-loop configuration.

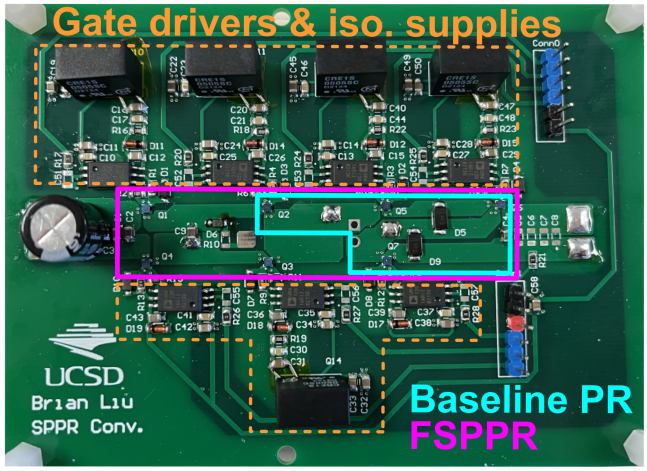

(a)

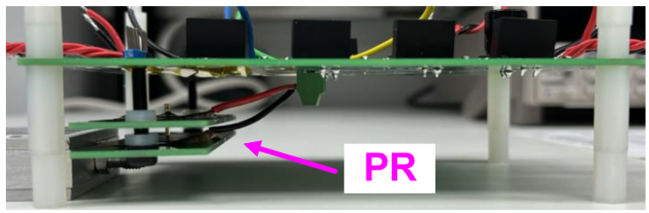

(b)

Fig. 15. Prototype of frontside series/parallel piezoelectric resonator converter. (a) Top view. (b) Side view.

TABLE V
Experimental Parts and Parameters

Parts/Parameters	Values	Implementation
Switches (S1-S7)	80 V, 10 A, 20 mΩ	EPC2214
S6,7 parallel diode	40 V, 2 A	PMEG4020EP
Gate driver	Isolated, 2.3 A	ADUM4120
Digital Controller	150 MHz	TMS320F28335
Piezoelectric Resonator	20/0.2 mm (Dia./thick.)	PIC181 material
Input voltage range V_{in}	36–48 V	–
Output voltage range V_o	4–10 V	–
Output current range I_o	0.05–0.3 A	–
flying capacitor C_1	4.7 μF	MLCC (0805)
Resonant frequency f_r	≈ 113 kHz	Piezo resonator
Anti-resonant frequency f_r	≈ 129 kHz	Piezo resonator
piezo-static capacitor C_P	13.96 nF	Piezo resonator
Mechanical capacitor C	4.2 nF	Piezo resonator
Mechanical Inductor L	468.78 μH	Piezo resonator
Mechanical resistor R	0.48 Ω	Piezo resonator
Quality factor Q	696	Piezo resonator

Since the PRs usually come with bare dies and are typically targeted for ultrasonic, acoustic, and actuator applications, there is no power-electronics-optimized PR with a standard package available on the market. Hence, the mounting of PRs plays a vital role in determining the converter's overall efficiency. That is, improper mounting can result in significant efficiency degradation. Here, the sandwich-like mounting method, illustrated in Fig. 16(a), is applied to this prototype that involves placing the PR between two nonconductive plates, each equipped with a copper plate as a conductive surface. The positive electrode of

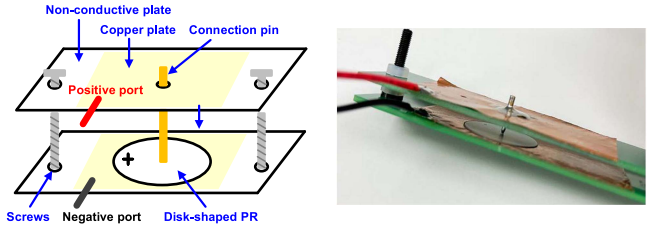

Fig. 16. Sandwich mounting for piezoelectric resonators. (a) 3-D view. (b) Implementation.

the PR is connected via a connection pin, while the negative electrode is in direct contact with the copper plate. Screws on each side of the nonconductive plates allow for contact adjustment, ensuring unclamped contact for a clean response (minimizing the occurrence of spurious modes). Fig. 16(b) provides an actual implementation using an FR4 PCB board as the nonconductive plate and golden micro pins as connection pins. The advantages of this sandwich mounting approach include nondestructive contact, flexibility, and protection against depolarization, aging, and damage caused by excessive heat and force during soldering and handling. Fine-tuning the PR position and screws allows for easy adjustment to the desired centered-pined and unclamped contact position, resulting in an ideal response.

Fig. 17 presents the impedance results of a piezoelectric resonator (PR), both across the full spectrum and within the zoomed-in radial mode spectrum, as measured by a vector network analyzer. Model-fitting results are also displayed alongside these measurements. According to the datasheet [36], for a PR size of 20/0.2 mm, the resonant frequencies for the radial and thickness modes are 113 kHz and 11 MHz, respectively. In the full spectrum measurement, the radial mode impedance appears high at its resonant frequency, a phenomenon attributable to the limited resolution available over a wide frequency range (50 kHz to 20 MHz). Therefore, the spectrum of interest (frequencies in the vicinity of the radial mode) is zoomed in, demonstrating a clean frequency response without spurious modes and a beautiful agreement between measurement and model fit results. It should be noted that mounting and packaging of PRs for use in dc–dc converters is an ongoing topic of research and development. Note that the model fitting specifically focuses on the radial model, and thereby, the thickness model is ignored. To include the thickness vibration and other harmonics, the modified BVD (MBVD) can be adopted [39].

The steady-state waveforms of the baseline PR-based converter and FSPPR converter are shown in Fig. 18. Fig. 18(a) and (b) depicts the waveform comparison of baseline PR-based and FSPPR converters at a 48/10 V conversion ratio, while Fig. 18(c) and (d) shows the comparison at a 36/8V conversion ratio. Analysis of the waveforms reveals that a longer input-to-output connected state duration (t_2) and a shorter current circulating shorted state duration (t_4) are exhibited in the FSPPR converter than in the baseline PR-based converter, where the definitions of t_2 and t_4 are presented in Fig. 7. This discrepancy suggests a higher utilization factor of the PR in the FSPPR converter, thereby implying the potential for higher efficiency. On the other

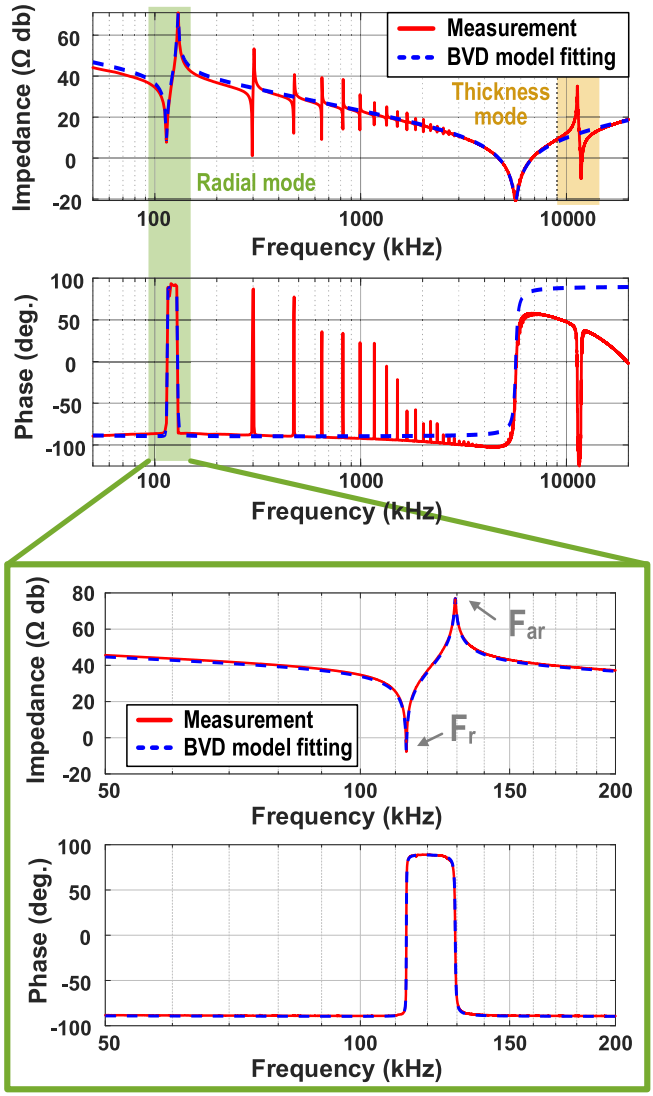

Fig. 17. Piezoelectric resonator impedance measured and model-fitting results.

hand, Fig. 18(b) and (d) shows the waveform comparison of the FSPPR converter at different input/output scenarios, which are 48/10 V and 36/8 V conversion ratio respectively. The V_{C1} waveforms in both cases present soft-charging/discharging of the flying capacitor (C_1), eliminating capacitor hard-switching losses. Moreover, ZVS has been achieved in both baseline PR-based and FSPPR converters, except for S1–4, where minor switching noise presents at the rising edge of V_{P2} in Fig. 18(b) and (d).

To evaluate the performance of the proposed topology and compare it with the baseline PR-based converter, multiple experiments are conducted with various operating points. Fig. 19 shows the comparisons of the baseline PR-based and FSPPR converters in terms of efficiency, input-output-connected state time duration, t_2, and frequency variation with different input/output conditions. Here, the efficiency is defined as (24) in a similar way as [20], [21], [26]. The efficiency measurement results are shown in Fig. 19(a)–(c), the t_2 results are demonstrated in Fig. 19(d)–(f), and the frequency variation results are

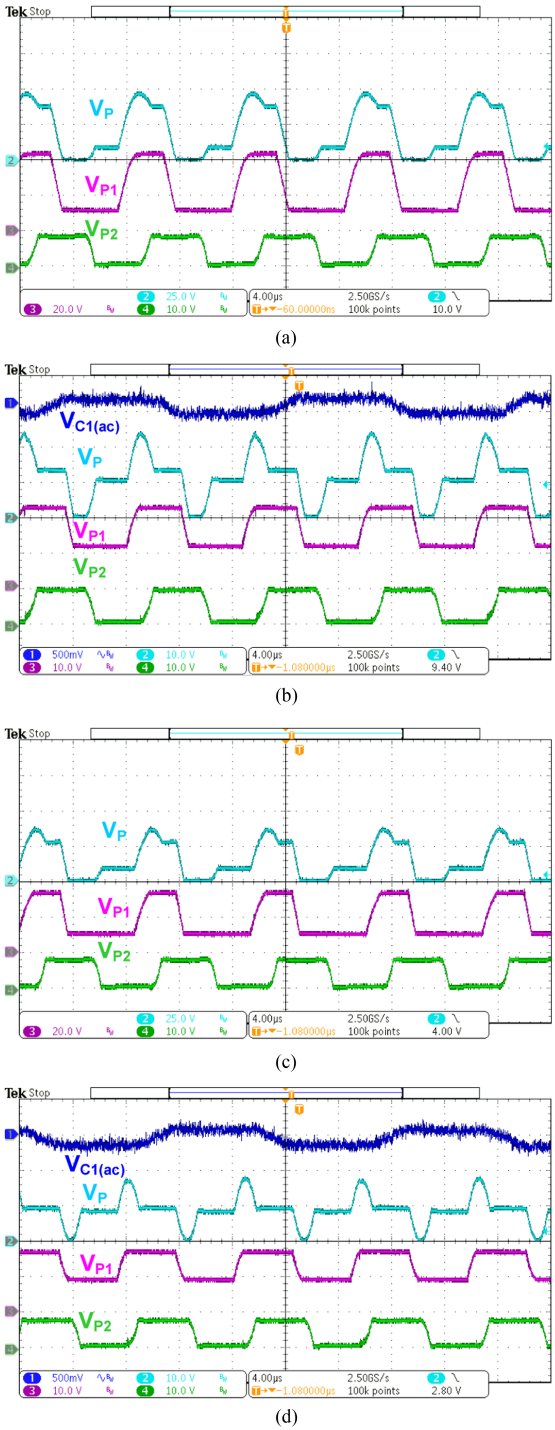

Fig. 18. Steady-state waveforms of baseline PR-based and FSPPR converters. (a) 48/10 V/0.25 A PR-based converter. (b) 48/10 V/0.25 A FSPPR converter. (c) 36/8 V/0.25 A PR-based converter. (d) 36/8 V/0.25 A FSPPR converter.

presented in Fig. 19(g)–(i). Note that the testing stops when the PR shows unstable behavior such as low-frequency oscillation and/or an output voltage drop over time. Based on the experimental stop points, the peak PR current, $I_{L,\mathrm{PR}(pk)}$, is limited to around 0.8–1 A, where the value is extrapolated from the model in Section III. Note that, the BVD resistance is adjusted based on different output power/current conditions due to the power limitation of VNA and future work will thoroughly investigate the effect of power/current level on BVD resistance.

Fig. 19(a) shows the efficiency comparison of the baseline PR-based and FSPPR converters at 48/10 V and 36/8,V conversion ratios. Here, the equivalent PR conversion ratio, $\mathrm{VCR_{PR}}$, of the FSPPR converter is 0.42 and 0.44 at 48/10 and 36/8 input/output voltages, respectively, compared to 0.21 and 0.22 of the baseline PR-based converter at the same input/out voltage. Because of a higher $\mathrm{VCR_{PR}}$, the FSPPR converter shows an enhanced performance to the baseline PR-based converter, where the peak efficiency is 95.27%, and the efficiency improvement is up to 14% at a 48/10 conversion ratio. The calculated efficiencies are also marked in the figure. As shown, compared to calculated efficiencies, the measurement results present differences in efficiency. The differences can be attributed to several factors: 1) open-loop operation, where the operation timing is exactly matched with the ideal operation. To prevent false action of the converter, the synchronous rectifiers are turned ON/OFF a little bit later/earlier, compared to the ideal case, introducing additional diode conduction/switching losses to the system, and it becomes worse in baseline PR-based converter cases due to a higher resonant current. 2) Harmonic and spurious mode excitation, were the PR current is not a pure sinusoidal wave that the harmonics excite other resonant modes, resulting in extra loss [20], [21], [26], and is hypothesized to affect the baseline converter more strongly due to its higher resonant current [26], [33], [40] limiting it's ability to deliver higher output current at large conversion ratios; however, an accurate model is not currently available to predict this behavior. 3) The difference in small-signal and large-signal behaviors; here, the PR parameters are assumed to be constant but, in reality, they vary with deformation (amplitude of $I_{L,\mathrm{PR}}$), temperature, aging, and other factors, leading to extra loss [14]. Collectively, these factors contribute to the observed deviation in measured efficiency from calculated values, particularly at higher power outputs [26] and lower PR conversion ratios [33], where $I_{L,\mathrm{PR}}$ amplitude is more significant. 4) Approximation in calculation, where several assumptions were made in the calculations, i.e., the resonant frequency approximation, and lossless system assumptions, causing the difference between calculation and measurement results.

To ensure that the baseline PR-based converter is optimally designed for comparison, the efficiencies at 24/10 V ($\approx$ 0.42 VCR) and 18/8 V ($\approx$0.44 VCR) are measured and compared with calculated results, as illustrated in Fig. 20. The measured efficiencies closely align with the calculated projections, confirming the optimal operations. Also, consistent with previous discussions, the discrepancy in efficiency rises with an increase in output power [26], where $I_{L,\mathrm{PR}}$ is increased as well.

Fig. 19(b) and (c) shows the efficiencies of the FSPPR converter at the 48 and 36 V input voltage with different output voltages and currents. The efficiency curves show a similar trend as in Fig. 10, where, at a given output current, the efficiency decreases with a decrease in conversion ratio. In addition, at low VCRs, the efficiency of the FSPPR converter outperforms the baseline PR-based converter.

Fig. 19(d) shows the input–output-connected time, t_2, comparison of the baseline PR-based and FSPPR converters. The

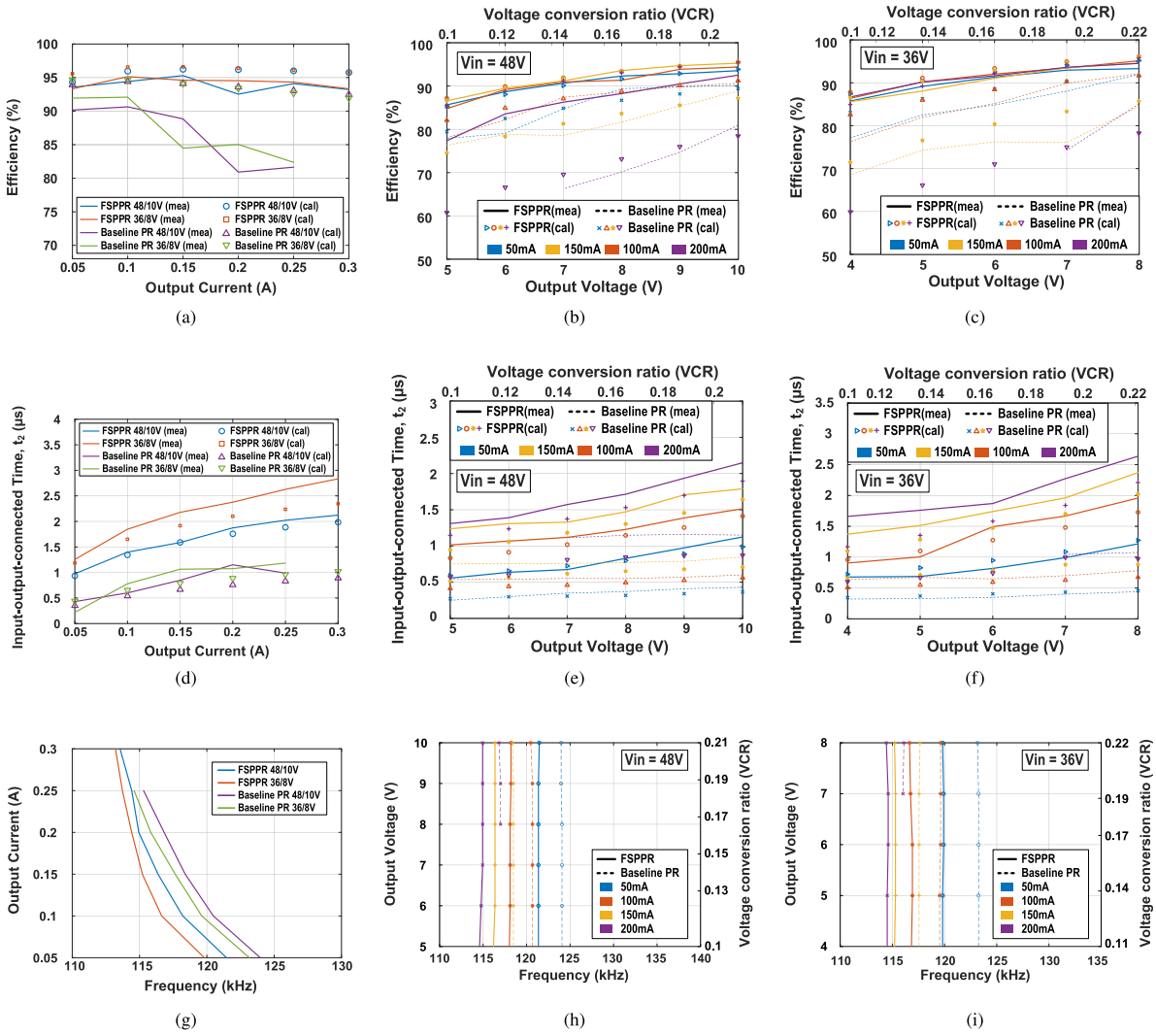

Fig. 19. Efficiency, input–output-connected time curves, and frequency variation: (a) Efficiency comparison of the baseline PR-based and FSPPR converters with calculation results, (b) Efficiencies of the baseline PR-based and FSPPR converters at 48 V input voltage, (c) Efficiencies of the baseline PR-based and FSPPR converters at 36 V input voltage, (d) Input–output-connected time comparison of the baseline PR-based and FSPPR converters with calculation results, (e) Input–output-connected time of the baseline PR-based and FSPPR converters at 48 V input voltage, (f) Input–output-connected time at of the baseline PR-based and FSPPR converters at 36 V input voltage, (g) frequency variation comparison of the baseline PR-based and FSPPR converters, (h) frequency variation of the baseline PR-based and FSPPR converters at 48 V input voltage, and (i) frequency variation of the baseline PR-based and FSPPR converters at 36 V input voltage.

input–output-connected state is phase 2 in Fig. 5, where the PR is connected to input and output at the same time, in which the input delivers power to the output through PR while PR stores energy in itself. As analyzed in (5) and [34], the duration of t_2 is used for the voltage regulation, and therefore, Fig. 19(d) shows that with an increase of the output current, which is equivalent to an increase of output power, t_2 increases accordingly to deliver more energy requested by the output. Besides, a portion of t_2 increase is to compensate for the voltage drop due to losses, as illustrated in (12). For example, as shown in Fig. 19(a), it can be seen that the efficiency of the baseline PR-based converter at a 48/10 V conversion ratio shows an efficiency drop at the output current of 0.2 A, and correspondingly, t_2 shows a sudden increase, as shown in Fig. 19(d), to maintain output regulation. The same trend is also shown in the baseline PR-based converter at a 36/8 V conversion ratio. The calculated t_2 is also marked in Fig. 19(d). The measurement results follow the same trend with calculation but with differences at some points. The discrepancy could result from many factors as mentioned above.

Fig. 19(g) shows the frequency variation comparison of the baseline PR-based and FSPPR converters at different output currents. It can be observed that the operation frequency ranges between resonant and anti-resonant frequency, f_r and f_{ar}, and decreases with an increase in output current/power due to the shorter opened states and longer connected states in both the baseline PR-based and FSPPR converters.

Fig. 19(h) and (i) shows the frequency variation of the FSPPR converter at 48 and 36 V input voltage with different output voltages. The operating frequency is fairly constant at a given output current regardless of the output voltage level. Although fairly constant operating frequency results are presented, the t_2 of the FSPPR converter at the input voltage of 48 and 36 V with different output is not constant, as shown in Fig. 19(e) and (f). This variation arises from differences in losses, conversion

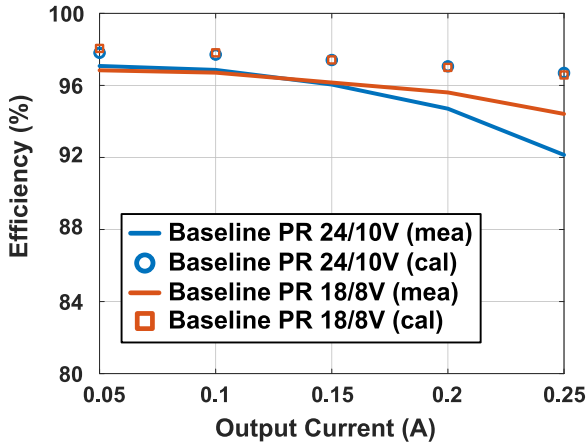

Fig. 20. Baseline PR-based converter efficiency at the vicinity of its optimal point: VCR ≈ 0.5 .

TABLE VI
PERFORMANCE COMPARISON TABLE

	Baseline PR [20]	FSPPR
Active footprint	5.8 mm^3 (4x GaN*)	10.2 mm^3 (7x GaN*)
Passive footprint	62.8 mm^3 (PR^+ only)	65.2 mm^3 (PR^+, 1x 0805 Cap.)
$P_{o(\max)}$	2.5 W	3 W
Power density	36.4 W/cm^3	39.8 W/cm^3
Input/output voltage range**	36–48/0–24 V ($0 \leq VCR \leq 0.5$)	36–48/0–12 V ($0 \leq \mathrm{VCR} \leq 0.25$)
Peak efficiency	92.08% (48/10 V, 0.1 A)	95.27% (48/10 V, 0.15 A)

*GaN: EPC2214 (20mΩ), + PR size(20/0.2mm) in diameter and thickness.
**assuming ideal operation

ratios, and PR utilization factors. As observed, t_2 increases with an increase in the VCR or output current, agreeing with the trend observed in Section III.

Table VI highlights the advantages of the FSPPR converter relative to the co-designed baseline PR-based converter with parameters shown in Table V. Despite the FSPPR featuring additional switches and a flying capacitor, its overall power density, denoted as $P_{o(\max)}$/(Total footprints), surpasses that of the baseline PR-based at low VCR (high-step-down ratio) scenarios. This is attributed to the hybrid SC, which enhanced the PR utilization factor in the FSPPR converter. Consequently, this enhancement leads to a reduction in $I_{L,\mathrm{PR}(pk)}$, thereby facilitating a higher output capacity while maintaining a compact footprint. The FSPPR thus achieves better peak efficiency and power density at low VCRs. Note that the baseline PR-based converter can operate with wider voltage range while the FSPPR converter is more advantageous at low VCRs.

VI. CONCLUSION

This article proposes a frontside series/parallel PR-based (FSPPR) dc–dc converter to improve the performance of conventional PR-based converters at low VCRs. By leveraging SC hybridization, the PRs can operate at their optimal conversion ratio, specifically, $\mathrm{VCR_{RP}} \approx 0.5$, all while maintaining an overall compact size and all of the advantages of PR-based converters, i.e., ZVS and soft-charging of capacitors. The operation, circuit behavior, and loss model of the proposed topology are presented, analyzed, and validated through simulation, calculation, and experiments. In addition, the size selection and mounting of the piezoelectric resonator are discussed, supported by calculation and measurement results. Finally, a FSPPR converter prototype is built with a disk-shaped PZT piezoelectric resonator operating in a radial vibration mode and can be reconfigured as a co-designed baseline PR-based converter for fair comparisons. The prototype demonstrates 95.27% peak efficiency with up to 14% efficiency improvement compared to the baseline PR-based converter at a 48/10 V conversion ratio. In summary, the analysis and measurement results highlight the piezoelectric resonator as a promising alternative to magnetic components for energy storage, offering new possibilities for power converter miniaturization.

REFERENCES

[1] C. R. Sullivan, B. A. Reese, A. L. F. Stein, and P. A. Kyaw, "On size and magnetics: Why small efficient power inductors are rare," in *Proc. Int. Symp. 3D Power Electron. Integration Manuf.*, 2016, pp. 1–23.
[2] D. J. Perreault et al., "Opportunities and challenges in very high frequency power conversion," in *Proc. 24th Annu. IEEE Appl. Power Electron. Conf. Expo.*, 2009, pp. 1–14.
[3] A. J. Hanson, J. A. Belk, S. Lim, C. R. Sullivan, and D. J. Perreault, "Measurements and performance factor comparisons of magnetic materials at high frequency," *IEEE Trans. Power Electron.*, vol. 31, no. 11, pp. 7909–7925, Nov. 2016.
[4] P. A. Kyaw, A. L. F. Stein, and C. R. Sullivan, "Fundamental examination of multiple potential passive component technologies for future power electronics," *IEEE Trans. Power Electron.*, vol. 33, no. 12, pp. 10708–10722, Dec. 2018.
[5] J. D. Boles, J. E. Bonavia, P. L. Acosta, Y. K. Ramadass, J. H. Lang, and D. J. Perreault, "Evaluating piezoelectric materials and vibration modes for power conversion," *IEEE Trans. Power Electron.*, vol. 37, no. 3, pp. 3374–3390, Mar. 2022.
[6] S. A. Chandorkar, M. Agarwal, R. Melamud, R. N. Candler, K. E. Goodson, and T. W. Kenny, "Limits of quality factor in bulk-mode micromechanical resonators," in *Proc. IEEE 21st Int. Conf. Micro Electro Mech. Syst.*, 2008, pp. 74–77.
[7] M. Touhami et al., "Piezoelectric materials for the DC-DC converters based on piezoelectric resonators," in *Proc. IEEE 22nd Workshop Control Modelling Power Electron.*, 2021, pp. 1–8.
[8] E. Horsley, M. Foster, and D. Stone, "State-of-the-art piezoelectric transformer technology," in *Proc. Eur. Conf. Power Electron. Appl.*, 2007, pp. 1–10.
[9] C. Lin and F. Lee, "Design of a piezoelectric transformer converter and its matching networks," in *Proc. 1994 Power Electron. Specialist Conf.*, 1994, vol. 1, pp. 607–612.
[10] M. Prieto, J. Diaz, J. Martin, and F. Nuno, "A very simple dc/dc converter using piezoelectric transformer," in *Proc. IEEE 32nd Annu. Power Electron. Specialists Conf. (IEEE Cat. No.01CH37230)*, 2001, vol. 4, pp. 1755–1760.
[11] L. Wang, Q. Wang, M. Khanna, R. P. Burgos, K. D. Ngo, and A. V. Carazo, "Design and control of tunable piezoelectric transformer based DC/DC converter," in *Proc. IEEE Energy Convers. Congr. Expo.*, 2018, pp. 5987–5993.
[12] Y.-K. Lo and K.-J. Pai, "Feedback design of a piezoelectric transformer-based half-bridge resonant CCFL inverter," in *Proc. Int. Aegean Conf. Elect. Machines Power Electron.*, 2007, pp. 162–167.
[13] E. L. Horsley, A. V. Carazo, N. Nguyen-Quang, M. P. Foster, and D. A. Stone, "Analysis of inductorless zero-voltage-switching piezoelectric transformer-based converters," *IEEE Trans. Power Electron.*, vol. 27, no. 5, pp. 2471–2483, May 2012.

[14] J. D. Boles, E. Ng, J. H. Lang, and D. J. Perreault, "DC-DC converter implementations based on piezoelectric transformers," *IEEE Trans. Emerg. Sel. Topics Power Electron.*, vol. 10, no. 6, pp. 6754–6769, Dec. 2022.
[15] M. P. Foster, J. N. Davidson, E. L. Horsley, and D. A. Stone, "Critical design criterion for achieving zero voltage switching in inductorless half-bridge-driven piezoelectric-transformer-based power supplies," *IEEE Trans. Power Electron.*, vol. 31, no. 7, pp. 5057–5066, Jul. 2016.
[16] D. Vasic, Y.-P. Liu, F. Costa, and D. Schwander, "Piezoelectric transformer-based DC/DC converter with improved burst-mode control," in *Proc. IEEE Energy Convers. Congr. Expo.*, 2013, pp. 140–146.
[17] M. Sanz, P. Alou, A. Soto, R. Prieto, J. Cobos, and J. Uceda, "Magnetic-less converter based on piezoelectric transformers for step-down dc/dc and low power application," in *Proc. 18th Annu. IEEE Appl. Power Electron. Conf. Expo.*, 2003, vol. 2, pp. 615–621.
[18] M. Ekhtiari, Z. Zhang, and M. A. E. Andersen, "State-of-the-art piezoelectric transformer-based switch mode power supplies," in *Proc. IECON 2014-40th Annu. Conf. IEEE Ind. Electron. Soc.*, 2014, pp. 5072–5078.
[19] M. Touhami, G. Despesse, and F. Costa, "A new topology of DC-DC converter based on piezoelectric resonator," *IEEE Trans. Power Electron.*, vol. 37, no. 6, pp. 6986–7000, Jun. 2022.
[20] J. D. Boles, J. J. Piel, and D. J. Perreault, "Enumeration and analysis of DC-DC converter implementations based on piezoelectric resonators," *IEEE Trans. Power Electron.*, vol. 36, no. 1, pp. 129–145, Jan. 2021.
[21] W. D. Braun et al., "Optimized resonators for piezoelectric power conversion," *IEEE Open J. Power Electron.*, vol. 2, pp. 212–224, 2021.
[22] J. D. Boles, J. E. Bonavia, J. H. Lang, and D. J. Perreault, "A piezoelectric-resonator-based DC-DC converter demonstrating 1 kw/cm resonator power density," *IEEE Trans. Power Electron.*, vol. 38, no. 3, pp. 2811–2815, Mar. 2023.
[23] E. Stolt, W. Braun, K. Nguyen, V. Chulukhadze, R. Lu, and J. Rivas-Davila, "A spurious-free piezoelectric resonator based 3.2 kw DC-DC converter for EV on-board chargers," *IEEE Trans. Power Electron.*, vol. 39, no. 2, pp. 2478–2488, Feb. 2024.
[24] V. Breton, E. Bigot, G. Despesse, and F. Costa, "A new isolated topology of DC-DC converter based on piezoelectric resonators," *IEEE Trans. Power Electron.*, vol. 38, no. 8, pp. 10012–10025, Aug. 2023.
[25] K. Van Dyke, "The piezo-electric resonator and its equivalent network," *Proc. Inst. Radio Eng.*, vol. 16, no. 6, pp. 742–764, 1928.
[26] B. Pollet, G. Despesse, and F. Costa, "A new non-isolated low-power inductorless piezoelectric DC-DC converter," *IEEE Trans. Power Electron.*, vol. 34, no. 11, pp. 11002–11013, Nov. 2019.
[27] W.-C. B. Liu and P. P. Mercier, "A series/parallel magnetic-less step-down converter based on piezoelectric resonators," in *Proc. IEEE Appl. Power Electron. Conf. Expo.*, 2023, pp. 484–489.
[28] Q. Li, Y. Hou, and K. K. Afridi, "Merged switched-capacitor piezoelectric-resonator based DC-DC converter with high voltage conversion ratio," in *Proc. IEEE 24th Workshop Control Model. Power Electron.*, 2023, pp. 1–8.
[29] W.-C. B. Liu and P. P. Mercier, "A merged backside series/parallel hybrid piezoelectric-resonator-based DC-DC converter," in *Proc. IEEE Appl. Power Electron. Conf. Expo.*, 2024, pp. 2130–2135.
[30] W.-C. B. Liu, G. Pillonnet, and P. P. Mercier, "8.6 an integrated dual-side series/parallel piezoelectric resonator-based 20-to-2.2V DC-DC converter achieving a 310% loss reduction," in *Proc. IEEE Int. Solid-State Circuits Conf.*, 2024, vol. 67, pp. 364–366.
[31] J. D. Boles, P. L. Acosta, Y. K. Ramadass, J. H. Lang, and D. J. Perreault, "Evaluating piezoelectric materials for power conversion," in *Proc. IEEE 21st Workshop Control Model. Power Electron.*, 2020, pp. 1–8.
[32] B. Pollet, F. Costa, and G. Despesse, "A new inductorless DC-DC piezoelectric flyback converter," in *Proc. IEEE Int. Conf. Ind. Technol.*, 2018, pp. 585–590.
[33] W. D. Braun, Z. Tong, and J. Rivas-Davila, "Inductorless soft switching DC-DC converter with an optimized piezoelectric resonator," in *Proc. IEEE Appl. Power Electron. Conf. Expo.*, 2020, pp. 2272–2278.
[34] M. Touhami, G. Despesse, F. Costa, and B. Pollet, "Implementation of control strategy for step-down DC-DC converter based on piezoelectric resonator," in *Proc. 22nd Eur. Conf. Power Electron. Appl. (EPE'20 ECCE Europe)*, 2020, pp. 1–9.
[35] L. d. A. Pereira, A. Morel, M. Touhami, T. Lamorelle, G. Despesse, and G. Pillonnet, "Operating frequency prediction of piezoelectric DC-DC converters," *IEEE Trans. Power Electron.*, vol. 37, no. 3, pp. 2508–2512, Mar. 2022.
[36] Physik instrumente pzt material datasheet. [Online]. Available: https://www.pi-usa.us/fileadmin/user_upload/pi_us/files/catalogs/Piezo_Ceramics_Piezo_Materials_Piezo_Technology_Catalog-PIC.pdf
[37] J. Erhart, P. Plpán, and M. Pustka, *Piezoelectric Ceramic Resonators*. Berlin, Germany: Springer, 2017.
[38] R. Hou, J. Lu, and D. Chen, "Parasitic capacitance eqoss loss mechanism, calculation, and measurement in hard-switching for gan hemts," in *Proc. IEEE Appl. Power Electron. Conf. Expo.*, 2018, pp. 919–924.
[39] R. Lu, M.-H. Li, Y. Yang, T. Manzaneque, and S. Gong, "Accurate extraction of large electromechanical coupling in piezoelectric mems resonators," *J. Microelectromech. Syst.*, vol. 28, no. 2, pp. 209–218, 2019.
[40] E. Ng, J. D. Boles, J. H. Lang, and D. J. Perreault, "Non-isolated DC-DC converter implementations based on piezoelectric transformers," in *Proc. IEEE Energy Convers. Congr. Expo.*, 2021, pp. 1749–1756.

Wen-Chin B. Liu (Graduate Student Member, IEEE) received the B.S. degree in electronic and computer engineering from National Taiwan University of Science and Technology (NTUST), Taipei, Taiwan, in 2017, the M.S. degree in electrical engineering from National Taiwan University (NTU), Taipei, Taiwan, in 2019. He is currently working toward the Ph.D. degree in the electrical and computer engineering with the University of California San Diego (UCSD), CA, USA.

His current research interests include modeling, analysis, and control strategies of dc–dc converters for point-of-load applications, high-frequency, high-power-density dc-dc converters, PV-battery microgrid systems, and piezoelectric resonator-based dc–dc converters.

Patrick P. Mercier (Senior Member, IEEE) received the B.Sc. degree in electrical and computer engineering from the University of Alberta, Edmonton, AB, Canada, in 2006, and the S.M. and Ph.D. degrees in electrical engineering and computer science from the Massachusetts Institute of Technology (MIT), Cambridge, MA, USA, in 2008 and 2012, respectively.

He is currently a Professor and Vice Chair of Electrical and Computer Engineering with the University of California San Diego (UCSD), where he is also the co-Director of the Center for Wearable Sensors and the Site Director of the Power Management Integration Center. His research interests include the design of energy-efficient microsystems, focusing on the design of RF circuits, power converters, and sensor interfaces for miniaturized systems and biomedical applications.

Prof. Mercier authored or coauthored more than 200 peer-reviewed papers, including 26 ISSCC papers, 34 JSSC papers, and several papers in high-impact journals such as Science, Nature Biotechnology, Nature Biomedical Engineering, Nature Electronics, Nature Communications, Advanced Science, and more. He was a recipient of numerous awards, including a Natural Sciences and Engineering Council of Canada (NSERC) Julie Payette fellowship in 2006, NSERC Postgraduate Scholarships in 2007 and 2009, an Intel Ph.D. Fellowship in 2009, the IEEE International Solid-State Circuits Conference (ISSCC) Jack Kilby Award for Outstanding Student Paper at ISSCC 2010, a Graduate Teaching Award in Electrical and Computer Engineering at UCSD in 2013, the Hellman Fellowship Award in 2014, the Beckman Young Investigator Award in 2015, the DARPA Young Faculty Award in 2015, the UC San Diego Academic Senate Distinguished Teaching Award in 2016, the Biocom Catalyst Award in 2017, the NSF CAREER Award in 2018, a National Academy of Engineering Frontiers of Engineering Lecture in 2019, the San Diego County Engineering Council Outstanding Engineer Award in 2020, the ISSCC Author Recognition Award in 2023, and the ECE Teacher of the Year award in 2023. He was an Associate Editor of IEEE TRANSACTIONS ON VERY LARGE SCALE INTEGRATION (TVLSI), IEEE TRANSACTIONS ON BIOMEDICAL CIRCUITS AND SYSTEMS (TBioCAS), and IEEE SOLID-STATE CIRCUITS LETTERS. He is currently a member of the Executive Committee of ISSCC, and has served on the technical program committees for ISSCC, CICC, and the VLSI Symposium. Prof. Mercier was the co-editor of Ultra-Low-Power Short Range Radios (Springer, 2015) Power Management Integrated Circuits (CRC Press, 2016), and High-Density Electrocortical Neural Interfaces (Academic Press, 2019).